

See discussions, stats, and author profiles for this publication at: <https://www.researchgate.net/publication/317759031>

# Numerical analysis of turbulent flow dynamics and heat transport in a round jet at supercritical conditions

Article in *International Journal of Heat and Fluid Flow* · August 2017

DOI: 10.1016/j.ijheatfluidflow.2017.06.007

CITATIONS

9

READS

309

5 authors, including:



**Florian Ries**

Technische Universität Darmstadt

20 PUBLICATIONS 45 CITATIONS

[SEE PROFILE](#)



**Pedro Obando**

Technische Universität Darmstadt

3 PUBLICATIONS 10 CITATIONS

[SEE PROFILE](#)



**A. Sadiki**

Technische Universität Darmstadt

224 PUBLICATIONS 2,479 CITATIONS

[SEE PROFILE](#)

Some of the authors of this publication are also working on these related projects:



OxyFuel Combustion [View project](#)



Multiphase -based modeling, simulation and experimental validation of mold filling and solidification of metalica melts [View project](#)

# Numerical analysis of turbulent flow dynamics and heat transport in a round jet at supercritical conditions.

Ries F., Obando P., Shevchuck I., Janicka J., Sadiki A.

*Institute of Energy and Power Plant Technology, Technische Universität Darmstadt,  
64287 Darmstadt, Germany*

---

## Abstract

Using a direct numerical simulation (DNS), a round jet of cryogenic nitrogen, which mimics the experiment by Mayer et al. (2003) [1] in terms of geometry, thermodynamics, and hydrodynamics, but at reduced Reynolds-Number ( $Re=5300$  based on the injection diameter), is investigated. The objectives of the present paper are: (1) **to reliably predict the turbulence statistics in order to investigate the physical mechanisms, that dominate the flow dynamics, and to investigate the fuel disintegration and mixture formation**, (2) to analyze the characteristics of heat transport phenomena of supercritical flows in order to determine parameter regimes **advantageous to mixing**, and (3) to provide a database for model development and validation that is difficult to obtain experimentally at such extreme thermodynamic conditions.

The correctness of the results has been established at two levels. First, **a grid-sensitivity study has been carried out to determine the resolution, which provides grid-independent turbulence statistics**. This ensures, that the quantities of interest depend only on the physics and are not affected by the numerical methods. Secondly, **numerical results have been compared to available experimental data of sub- and supercritical jets**. Assuming self-similarity, several characteristics of the jet, like spreading rate, density variations and thermodynamic properties have been assessed.

Finally, a comprehensive database including instantaneous flow and temperature fields, mean flow characteristics, turbulence properties along with turbulent kinetic energy budget, and heat flux has been made available. A link to heat flux transport modeling has been established to evaluate the suit-

---

*Email address:* `ries@ekt.tu-darmstadt.de` (Ries F.)

ability of some existing heat flux models as employed in such supercritical fluid flow.

*Keywords:* direct numerical simulation; turbulent round jet; supercritical fluid flow; turbulence dynamics; turbulent heat transport.

---

## 1. Introduction

Currently, there is a great interest in processes occurring under supercritical thermodynamic conditions, like in propulsion applications including rocket engines, gas turbines or diesel engines [2, 3, 4]. Thereby, a clear trend to operate at higher combustion chamber pressure is observed in order to favor the production of higher specific energy conversion rates along with the improvement of thermodynamic performance. This is mainly achieved at pressures exceeding the critical pressures.

Under subcritical conditions, the injected fuel disintegrates due to the action of surface tension, which induces ligament formation, atomization and evaporating droplet with sharp interfaces. Once supercritical condition is reached, the breakup is replaced by mixing, including turbulent mixing and diffusion, as surface tension vanishes. As pointed out in [5], this leads researchers to consider continuous Eulerian mixing models instead of Lagrangian droplet tracking methods to deal with supercritical fluid flow.

In this respect, it is worth mentioning that the transition between supercritical liquid-like and gas-like states resembles subcritical vaporization. However, as pointed out in [6], the isothermal vaporization is replaced by a continuous non-equilibrium process at supercritical pressures. High pressure real fluid effects merely distribute the latent heat over a finite temperature interval and the thermal energy supplied is used to increase the temperature and overcome molecular forces simultaneously. In the literature, this process is known as pseudo-boiling [7, 6]. Thereby, the coexistence line between the liquid and gaseous phases is extended beyond the critical point by the so-called Widom line, a line which divides the liquid-like and gas-like supercritical states. Along the Widom line, the isothermal compressibility and the density gradient with respect to temperature and the specific heat capacity along with further thermodynamic properties exhibit maximal values. For such extremely complex phenomena, a satisfactory understanding is still needed, even though significant progress has been reported in the literature either in experiments [8, 9, 10, 11] or in the context of numerical modeling

[12, 13, 14, 15].

Several researchers applied RANS [1, 16, 17] or LES [12, 18, 19, 20] to gain more reliable predictions for practical applications. The main objective of these contributions was to evaluate the impact of selected SGS models and real gas equations of state on the mixing prediction. The effect on the subsequent combustion has also been addressed in [13, 21, 22, 23]. Especially the effects of equations of state for turbulent flows under supercritical thermodynamic conditions and their impact on modeling strategy have been addressed in [24, 25]. Okong'o et al. (2000) [26] and others [27, 28, 29, 30, 31] considered the supercritical issues in LES modeling using DNS. Such three dimensional DNS contributions as reported in the literature all reduced the Reynolds number owing to limited computational resources.

Recently, Ruiz et al. (2016) [32] used a two-dimensional DNS to provide a numerical benchmark for high-Reynolds-number supercritical flows with large density gradients in simple configurations containing the essential features of real devices (geometry, thermodynamics, and hydrodynamics). This DNS refers to a mixing layer forming downstream of an injector lip separating a stream of dense oxygen from a stream of light hydrogen, mimicking one experiment by Chehroudi et al. (2002) [33]. The authors provided mean and rms velocity, temperature profiles, power spectrum density of the square of transverse velocity, dense core lengths, mixing layer thickness, etc.

Focusing essentially on flow and mixing process, the so-called Mayer et al. (2003) configuration [1] and the Mascotte benchmark test [34, 35] have been widely investigated by means of LES (e.g. [18, 19, 20, 36]) with the main objective to evaluate the impact of selected SGS models known in subcritical environments and of the real gas equations of state on the mixing prediction. However, impeded by the lack of comprehensive and reliable validation data, the appraisal of the results and models used remains inconclusive.

A three dimensional DNS of such configurations appears therefore particularly important. Using a highly-resolved numerical simulation technique, a round jet of nitrogen, which mimics the experiment by Mayer et al. (2003) [1] in terms of geometry, thermodynamics, and hydrodynamics but at reduced Reynolds-Number is simulated in the present work. Thereby, the original Reynolds number of the experiment is reduced from  $Re = 1.62 \times 10^5$  (based on the injection diameter) to  $Re = 5300$  in the numerical study. A grid-sensitivity study has been carried out to prove the reliability of the results and to ensure that the quantities of interest depend only on the physics and not on the numerical approach.

The aims of the present study are: (1) to reliably predict the turbulence statistics in order to investigate the physical mechanisms that dominate the flow dynamics, and to investigate the fuel disintegration and mixture formation, (2) to analyze the characteristics of heat transport phenomena of supercritical flows in order to determine parameter regimes advantageous to mixing, and (3) to provide a database for model development and validation that is very difficult to obtain experimentally at such extreme thermodynamic conditions.

Section 2 introduces the theoretical framework, which includes governing equations and appropriate conservation laws, real fluid thermodynamics and transport properties over the entire temperature and pressure regime under consideration. Subsequently, the numerical procedure is outlined. Section 3 describes the test case under investigation along with the operating conditions and the initial and boundary conditions. The results are presented and discussed in section 4. With respect to the objectives, the results are provided in terms of instantaneous flow and temperature fields, mean flow characteristics, turbulence properties along with turbulent kinetic energy budget, and heat flux. These data are used to evaluate the suitability of some existing heat flux models as applied in such supercritical fluids.

## 2. Methods

In this section, governing equations, thermodynamic models and numerical methods used to simulate supercritical fluid flows are presented. A low Mach-number approach is employed, suitable for flows under incompressible conditions ( $Ma \ll 0.3$ ) and variable physical properties. In contrast to a fully compressible formulation, the pressure and density are formally decoupled by defining the density through an equation of state expressed in terms of local temperature  $T$  and thermodynamic pressure  $p^{th}$ . **Thereby acoustic and compressibility effects are neglected [37].**

### 2.1. Governing equations

In the case of incompressible fluid flow with variable physical properties and no gravity force, the employed governing equations of continuity, momentum and enthalpy are

$$\frac{\partial \rho}{\partial t} + \frac{\partial (\rho U_i)}{\partial x_i} = 0, \quad (1)$$

$$\frac{\partial (\rho U_i)}{\partial t} + \frac{\partial (\rho U_i U_j)}{\partial x_j} = -\frac{\partial p}{\partial x_i} + \frac{\partial \tau_{ij}}{\partial x_j}, \quad (2)$$

$$\frac{\partial (\rho h)}{\partial t} + \frac{\partial (\rho U_i h)}{\partial x_j} = -\frac{\partial q_i}{\partial x_i} + \tau_{ij} \frac{\partial U_i}{\partial x_j}, \quad (3)$$

where  $\rho$  is the density,  $U_i$  the velocity,  $p$  the pressure,  $\tau_{ij}$  the viscous stress tensor,  $h$  the sensible enthalpy, and  $q_i$  the heat flux. Assuming Newtonian fluid flow, the viscous stress tensor is modeled as

$$\tau_{ij} = \mu \left( \frac{\partial U_i}{\partial x_j} + \frac{\partial U_j}{\partial x_i} - \frac{2}{3} \frac{\partial U_k}{\partial x_k} \delta_{ij} \right), \quad (4)$$

where  $\mu$  is the molecular viscosity. The heat flux is expressed by Fourier's law assuming incompressible fluid flow

$$q_i = -\lambda \frac{\partial T}{\partial x_i} = -\frac{\lambda}{c_p} \frac{\partial h}{\partial x_i}, \quad (5)$$

where  $\lambda$  is the thermal conductivity and  $c_p$  the heat capacity of the fluid.

### 2.2. Thermodynamic models

To account for non-ideal gas behavior at supercritical conditions, the commonly used Peng-Robinson equation of state [38] (PR-EOS) is applied in the present study. The PR-EOS is represented as

$$p^{th} = \frac{RT}{v_{PR} - b} - \frac{a(T)}{v_{PR}(v_{PR} + b) + b(v_{PR} - b)}, \quad (6)$$

with

$$a(T) = 0.45724 \frac{R^2 T_c^2}{p_c} \left( 1 + \kappa \left( 1 - \sqrt{T/T_c} \right) \right)^2, \quad (7)$$

$$b = 0.07780 \frac{RT_c}{p_c}, \quad (8)$$

$$\kappa = 0.37464 + 1.54226\omega - 0.26992\omega^2. \quad (9)$$

Here,  $R$  is the molecular gas constant,  $v_{PR}$  the molar volume,  $T_c$  the critical temperature,  $p_c$  the critical pressure and  $\omega$  is the Pitzer acentric factor. It is well known, that the PR-EOS yields poor prediction for liquid density, especially at operating conditions near the critical point [39, 40]. To remedy this limitation, a generalized volume-translation method proposed by Abudour et al. (2012) [40] is employed in the present study.

In order to close the governing equations 1-5, expressions for  $h$ ,  $c_p$ ,  $\mu$  and  $\lambda$  in respect to temperature and thermodynamic pressure are required. By means of Maxwell's relations, the sensible enthalpy can be written as

$$h(T, p^{th}) = h^0(T) + \Delta h^{dep} = h^0(T) + \int_{p_0}^{p^{th}} \left( -T \left( \frac{\partial v_{PR}}{\partial T} \right)_p + v_{PR} \right) dp, \quad (10)$$

where  $h^0(T)$  refers to the enthalpy at standard pressure estimated using 7-coefficient NASA polynomials in the present study, whereas the departure functions  $\Delta h^{dep}$  are derived from the PR-EOS. By means of sensible enthalpy, isobaric heat capacity is calculated as  $c_p = (\partial h / \partial T)_{p^{th}}$ . Regarding transport properties at supercritical conditions, the correlations of Chung et al. (1988) [41] are applied for viscosity and thermal conductivity.

### 2.3. Numerical procedure

A segregated iterative solution approach, added to the open source C++ library OpenFOAM 2.4.0, is employed to solve fluid flow with variable physical properties. The low-Mach number equations (eq. 1-3) are generally solved using a series of predictor-corrector steps. Thereby, a merged PISO[42]-SIMPLE[43] algorithm is applied for coupling velocity and pressure. A schematic representation of the solution algorithm is shown in figure 1.

First, a density predictor is solved by means of the continuity equation with face fluxes of the previous time step. Then, the momentum equation including the pressure gradient from the previous iteration is calculated. Next, the enthalpy equation is computed and temperature is iteratively determined. Subsequently, the thermodynamic properties are updated by means of temperature and thermodynamic pressure  $p^{th}$  and in the last step, the pressure equation is solved and the velocity is corrected. The procedure is repeated (SIMPLE, PISO loops) until convergence is reached.

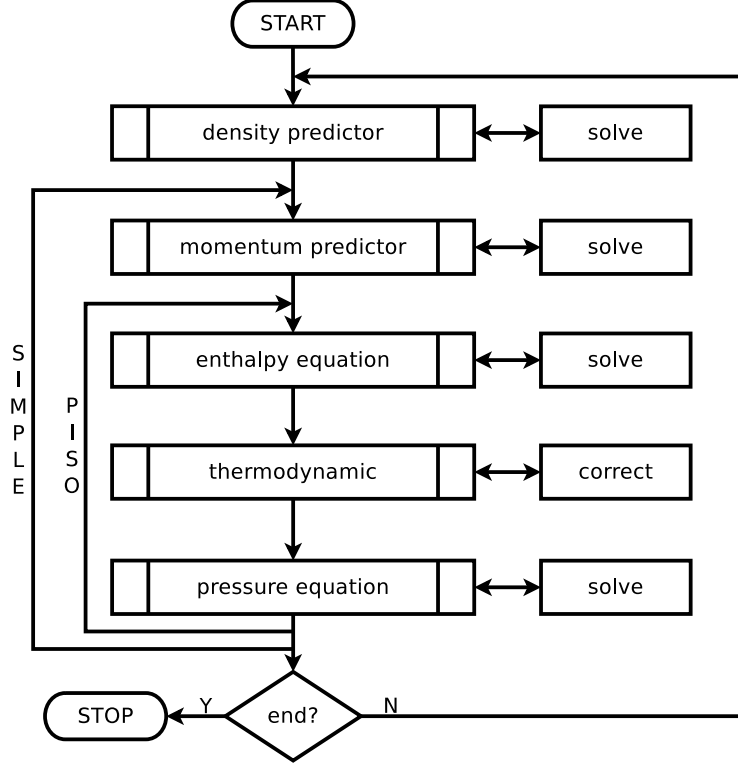


Figure 1: Flowchart of the low-Mach number PISO[42]-SIMPLE[43] solution algorithm.

The pressure Poisson equation of the low-Mach number solution approach is derived from the continuity and the discretized momentum equation and can be written as follows

$$\frac{\partial}{\partial x_i} \left( \rho a_p^{-1} \frac{\partial p}{\partial x_i} \right) = \frac{\partial}{\partial x_i} (\rho H a_p^{-1}) + \frac{\partial \rho}{\partial t}, \quad (11)$$

where  $a_p$  denotes the coefficient matrix of the discretized momentum equation and  $H$  consists of the off-diagonal coefficient matrix multiplied by corresponding velocities and all source terms apart from the pressure gradient [42, 44].

Regarding spatial and temporal discretization, a second order central differencing scheme is utilized for the convection terms and a second order, conservative scheme for the Laplacian terms. In the case of enthalpy fluxes, a second order minmod differencing scheme [45] is applied. A second order backward integration method is utilized for the time derivative terms. Geo-



metric agglomerated algebraic multigrid solvers are applied for the resolution of the pressure, momentum and enthalpy equations, whereas a preconditioned conjugate gradient solver is applied for the density predictor. Details about the discretization procedure and the numerical schemes can be found in the OpenFOAM Programmer’s guide [46].

### 3. Test case

In accordance with the experimental study of Mayer et. al. (2003) [1] (Case 3), a cryogenic round nitrogen jet injected into a cylindrical chamber is examined. The chamber has a length of 1000mm, a diameter of 122mm and is filled with warm nitrogen at supercritical pressure. The cold jet emanates from a fully developed turbulent pipe flow with a diameter of  $D = 2.2mm$  at  $Re = 1.62 \times 10^5$ . In contrast to the experiment, a lower inlet velocity is chosen in the present numerical study leading to a lower Reynolds-number of 5300, whereas the geometry of the configuration and the thermodynamic operating conditions are equal to the experimental investigation. It is evident, that the turbulent structures of the flow differ for different Reynolds numbers. However, as shown in several experimental and numerical studies of subcritical jets [47, 48, 49, 50, 51, 52], also at moderate Reynolds numbers ( $Re < 5000$ ), various characteristics of a jet, e.g. spreading rate, mean flow and thermodynamic properties, are independent of the Reynolds number beyond 20 jet diameters downstream of the jet exit. This might not be the case for all characteristics of a jet in supercritical flows, as shown below. Therefore, the experimental data of Mayer et. al. (2003) [1] are used for qualitative comparison only.

#### 3.1. Computational domain

Only a small portion of the experimental chamber, corresponding to the region of interest, is simulated in the present study. The computational domain consists of an injection part with a length of 2D and a portion of the experimental chamber with a length of 32D. To capture the spreading of the jet and to avoid any influence of the boundary conditions, the diameter of the chamber portion is increased gradually from 5D at the injection region to 18D at the outflow.

A block-structured, three-dimensional numerical grid is employed. It is refined at the injection region and throughout the jet’s core. A systematic grid refinement study is conducted using four grids with different spatial

resolution. Therefore, the grid is refined in each direction by a factor of  $\sim 1.3$ . A representation of the numerical grid (mid-plane cut and front view) is shown in figure 2. Characteristic quantities of the numerical grids are summarized in table 1.

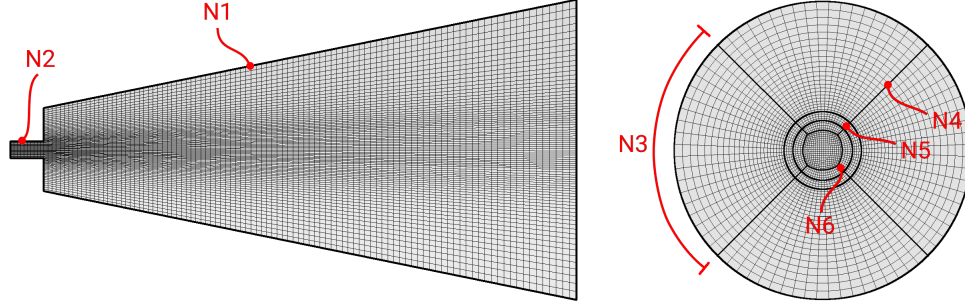


Figure 2: Representation of the numerical grid.

Table 1: Spatial resolution.  $N$  = total number of cells;  $N_i$  = cells along  $i=1,2,3\dots$

	grid 1	grid 2	grid 3	grid 4
$N$	4340740	9741400	22047740	48547410
$N_1$	310	404	525	689
$N_2$	62	81	110	138
$N_3$	39	51	66	86
$N_4$	36	47	61	80
$N_5$	23	30	40	50
$N_6$	21	27	37	46

### 3.2. Initial and boundary conditions

Realistic inflow turbulence is generated by a separate direct numerical simulation of a fully developed turbulent pipe flow. Thereby, slices of the instantaneous flow field are extracted from the middle section of the pipe domain for each time step and stored in a database. These data are interpolated with second order accuracy in space and time in order to match the inlet of the jet and utilized as inflow conditions of the jet simulation. At

the outflow, a velocity inlet/outlet boundary condition is imposed to allow entrainment of fluid from the surrounding. Thereby, incoming fluid velocity is obtained by the internal cell value, while Neumann condition is applied in the case outflow. At the walls, no-slip condition is utilized. In the case of temperature boundary conditions, Dirichlet condition is set for the inlet, while Neumann conditions are imposed at the outflows and the walls.

Regarding the separate numerical simulation of turbulent pipe flow, the diameter, bulk velocity and Reynolds number are equal to the cryogenic jet simulation. Periodic boundary conditions are applied in stream-wise direction and the pressure gradient, that drives the flow, is adjusted dynamically to maintain a constant mass flux. A computational domain with a length of  $L = 14D$  is used to resolve the maximum wavelengths of turbulent motions [53]. The numerical grid consists of 21714100 hexahedral cells with a non-dimensional grid spacing of  $r_{wall}^+ \times \Delta^+ \omega \times \Delta^+ z = 0.7 \times 5.2 \times 3.3$ . Figure 3 shows the predicted mean and rms velocities in respect to the non-dimensional wall distance  $r^+$ . For comparison, the DNS dataset of Ahn et al. [54] is utilized.

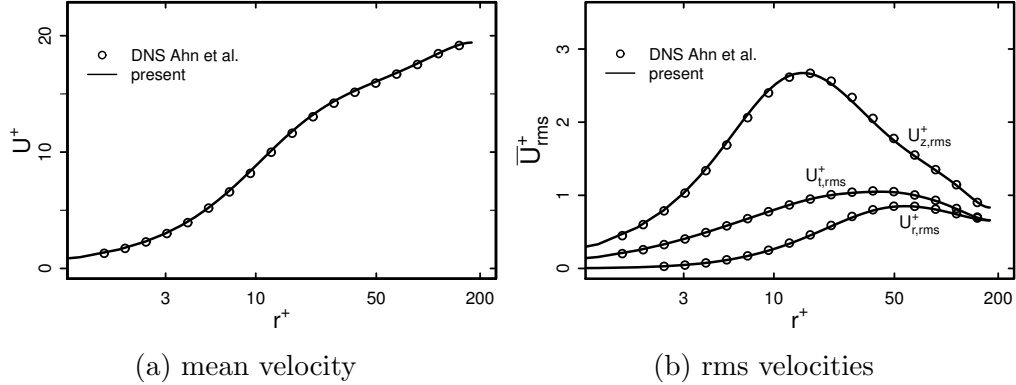


Figure 3: Mean and rms velocities of the turbulent pipe flow at  $Re_\tau = 180$  obtained from the present direct numerical simulation.

The mean and rms velocities are in excellent agreement with the reference DNS dataset, indicating appropriate spatial resolution. Therefore, accurate inflow conditions can be assumed for the present simulation of cryogenic nitrogen injection. Note that the recorded length of the inflow dataset and the duration of the jet simulation are identical.

In order to avoid uncertainties caused by the initial solution, the start-up phase of the jet simulation has to be long enough to ensure fully developed

turbulent flow. Similar to the start-up phase used in [52], sampling is started after 2 convective time scales, which is defined as  $t_c = 2 \cdot L_x / U_{inj}$ . Thereby,  $L_x$  is the length of the domain and  $U_{inj}$  is the injection velocity.

### 3.3. Operating conditions

Beside a robust numerical procedure, an accurate modeling of real gas effects is essential in numerical simulations of supercritical turbulent flows. For this reason, the thermodynamic models described in section 2.2 are compared with highly accurate reference data from the NIST chemistry webBook [55, 56] for nitrogen at a pressure of 3.98 MPa. Figure 4 shows the density, isobaric heat capacity, molecular viscosity and thermal diffusivity in respect to the temperature. The thermodynamic operating conditions of the jet and the chamber are highlighted in red.

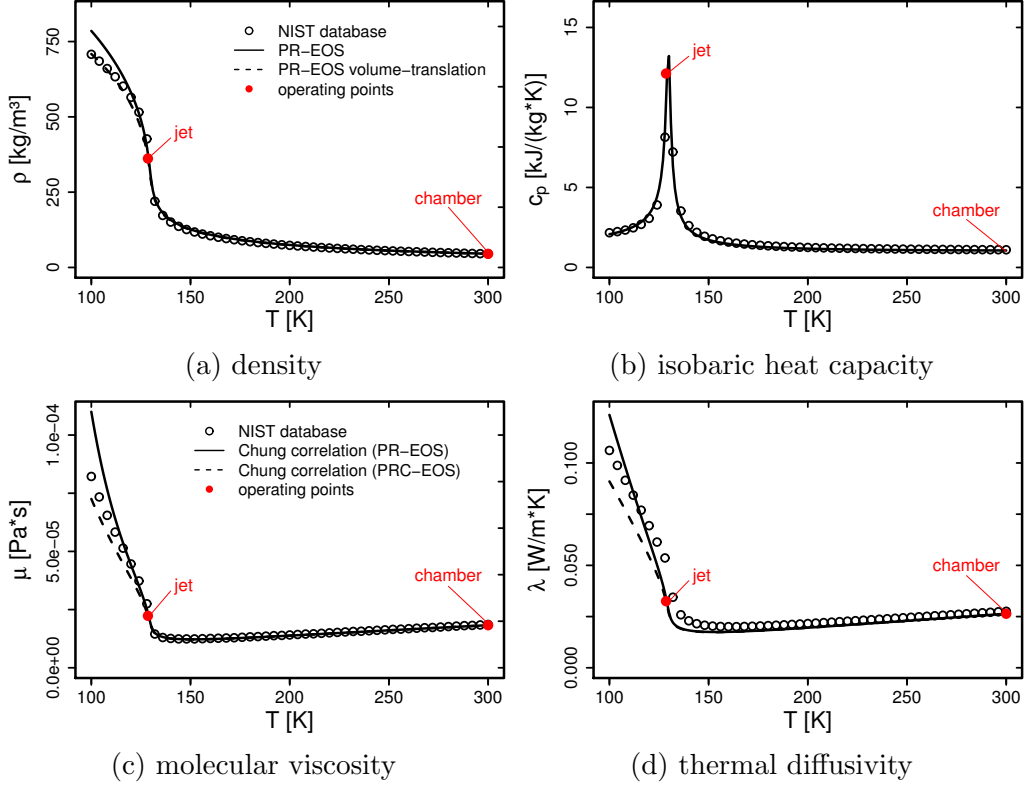


Figure 4: Validation of the thermodynamic models in respect to NIST database [55, 56]. Red symbols highlight the operating conditions of the simulation (jet and chamber).

The PR-EOS yields poor prediction for  $T < T_c$ , while nonideal gas behavior is well captured by the PR-EOS including the generalized volume-translation method in this region. Regarding transport properties, minor differences occur in the case of  $\mu$  and  $\lambda$ , that are slightly underestimated for temperatures below the critical temperature. However, in the range of the present operating conditions, the thermodynamic and transport models show a good agreement with the reference data and are therefore well applicable.

The thermodynamic and flow conditions of the supercritical nitrogen jet simulation are summarized in table 2.

Table 2: Operating and flow conditions of the direct numerical simulation.

property	description	value
$U_{inj}$	injection velocity	$0.151 \text{ m/s}$
$T_{inj}$	injection temperature	$128.53 \text{ K}$
$T_\infty$	chamber temperature	$298 \text{ K}$
$p^{th}$	chamber pressure	$3.98 \text{ MPa}$
$Re_{inj}$	injection Re-number	5300
$Ma_{inj}$	injection Ma-number	$0.71 \times 10^{-3}$

## 4. Results

Based on the thermo-physical models and numerical methods proposed in section 2, a direct numerical simulation of a cryogenic round jet at supercritical conditions is performed. First, a grid sensitivity study is presented in order to prove the reliability of the present results. Then, several instantaneous and statistical quantities of the flow field are analyzed. Afterwards, turbulent flow dynamics and heat transport are examined to gain further insight in the disintegration process of jets under supercritical thermodynamic conditions.

### 4.1. Grid sensitivity

Figure 5 depicts profiles of first and second order statistical moments of velocity and density for four different spatial resolutions (see table 1). Here and in the following,  $\widetilde{(\cdot)}$  denotes Favre-averaged values and  $(\cdot)''$  the fluctuation with respect to Favre average, while  $\overline{(\cdot)}$  and  $(\cdot)'$  correspond to Reynolds-averaged quantities. The root-mean-square of the density is defined

as  $\rho_{rms} = \sqrt{\overline{\rho' \rho'}}$  and of the turbulent velocity fluctuations as  $u_{rms} = \sqrt{2/3 \tilde{k}}$ , where  $\tilde{k} = 1/2 \widetilde{u_i'' u_i''}$  is the Favre-averaged turbulent kinetic energy. Statistics are averaged in time and in azimuthal direction.

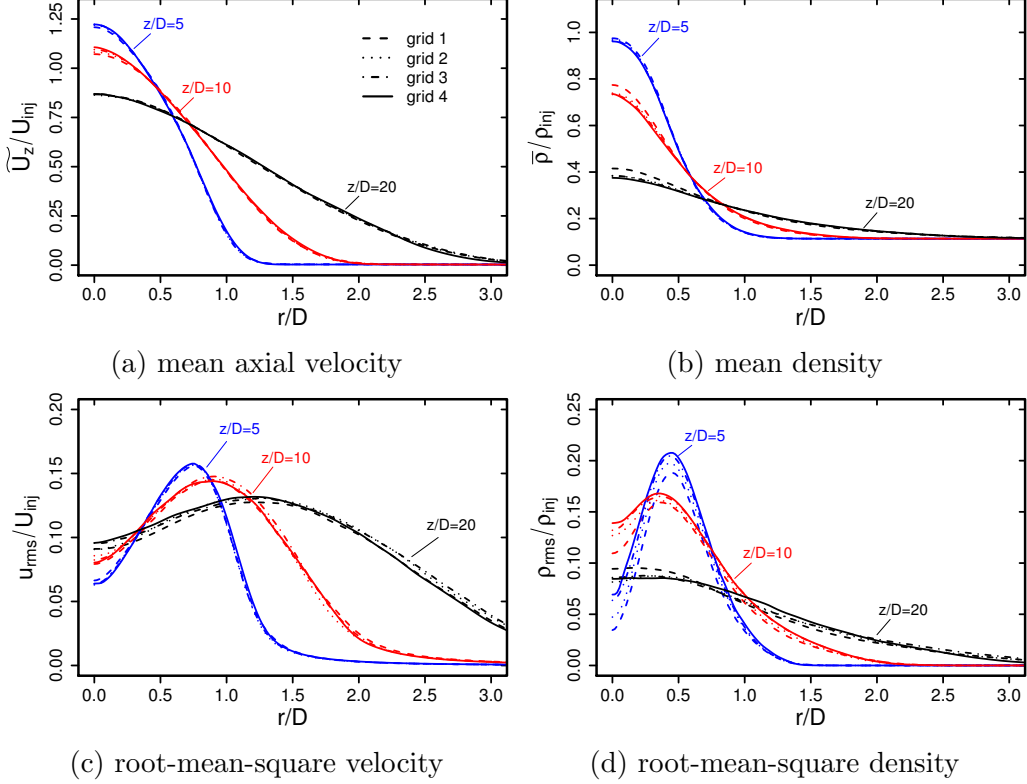


Figure 5: Mean and root-mean-square values of velocity and density profiles for four different spatial resolutions.

Regarding mean values, grid convergence is reached for grids 2, 3 and 4. Thereby, profiles of the velocity and density collapse onto a single curve, indicating grid independence. Grid 1 shows significant deviations, especially at the jet's axis. Results of second order statistical moments are a bit more affected by the spatial resolutions. For instance, peak values of density fluctuations are slightly underestimated in the case of low spatial resolution (grids 1 and 2). However, convergence is clearly reached, at least for the two highest spatial resolutions (grids 3 and 4).

Considering the commonly used DNS spatial resolution criterion, figure 6

displays the ratio of grid width  $\Delta = (\Delta_x \Delta_y \Delta_z)^{1/3}$  and the Kolmogorov length scale  $\eta = (\tilde{\nu}^3 / \tilde{\epsilon})^{1/4}$  along the centerline and in radial direction exemplarily at  $z/D = 20$ . Thereby  $\eta$  is computed for each location using the predicted local turbulent kinetic energy dissipation rate  $\tilde{\epsilon}$  and the local kinematic viscosity  $\tilde{\nu}$ . Following the guidelines in [57], sufficient spatial resolution is assumed if  $\Delta/\eta \leq \pi$ .

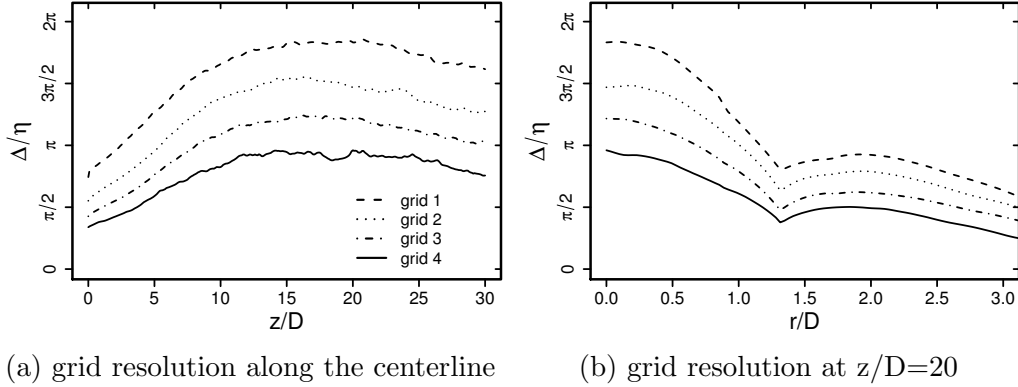


Figure 6: Ratio of grid width  $\Delta = (\Delta_x \Delta_y \Delta_z)^{1/3}$  and Kolmogorov length scale  $\eta$  (a) along the centerline and (b) in radial direction.

As expected, the ratio of grid width and Kolmogorov scale decreases with increasing spatial resolution. Highest values occur throughout the jet's axis, especially in the region  $10 > z/D > 25$ , while values are small close to the jet inflow and for large  $r/D$ . Regarding grids 1, 2 and 3, values of  $\Delta/\eta$  exceed the critical value of  $\pi$  in some regions of the domain, while in the case of finest mesh size (grid 4),  $\Delta/\eta \leq \pi$  is satisfied in the entire domain.

#### 4.2. Flow properties

Figure 7 displays the instantaneous magnitude velocity, temperature, magnitude density gradient and molecular Prandtl number ( $Pr = \mu c_p / \lambda$ ) fields at mid-plane section of the jet for  $2.5t_c$  (convective time scales) after the injection. Results are shown for the evolution of the jet up to  $z/D = 20$  in the ambient nitrogen. Red isolines in figure 7 (c) denote the mean density between the incoming and ambient nitrogen.

As the fully turbulent jet streams in the ambient nitrogen, the magnitude velocity decreases with increasing axial distance and the jet spreads in radial direction. In terms of the temperature field, it varies from low values

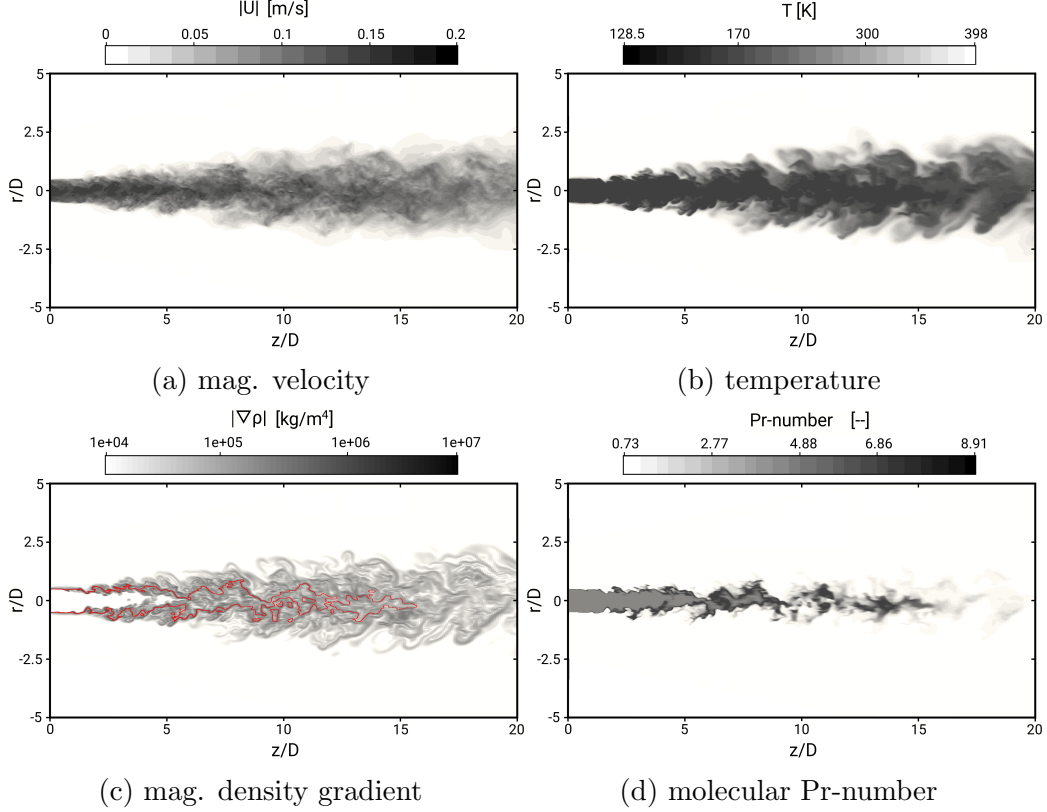


Figure 7: Snapshots of the magnitude velocity, temperature, magnitude density gradient and molecular Pr-number for  $2.5t_c$  (convective time scales) after the injection. Red isolines in (c) refers to the mean density between incoming and ambient nitrogen.

at the core of the jet to large values in the ambient nitrogen, whereby no truly sharp interface exists. Close to the inlet ( $z/D < 2$ ), the jet surface is almost unaffected by the surrounding. Further downstream, finger-like objects are formed due to stretching of the inner core by the shear layer of the jet. These temperature structures dissolve. This leads to a disintegration of the jet. Similar dynamics of supercritical jets were observed in experimental investigations [33, 9] and other DNS studies [58], in which turbulent mixing of a slightly supercritical Van der Waals fluid at low Mach number was examined. Regarding the density, sharp gradients occur at the interface between liquid-like cold jet and gas-like surrounding. Dense pockets of liquid-like nitrogen are separated from the jet core and tend to persist for a significant length downstream. This formation of dense pockets cannot be



ascribed to phase separation, due to the absence of surface tension at supercritical conditions. It is rather associated with poor thermal diffusivity and high isobaric heat capacity at the interface between cold liquid-like jet and warm gas-like ambient nitrogen resulting in high Pr-numbers. Thereby, the molecular Pr-numbers are approximately ten times higher at the jet interface than at the ambient nitrogen.

Regarding pseudo-boiling effects, figure 8 displays the isobaric heat capacity at four different cross sections ( $z/D=1, 5, 10, 15$ ) for  $2.5t_c$  after the injection. Thereby, pseudo-boiling is characterized by a maximum in specific heat capacity at supercritical pressure. Red isolines denote the mean density between the inlet and ambient nitrogen.

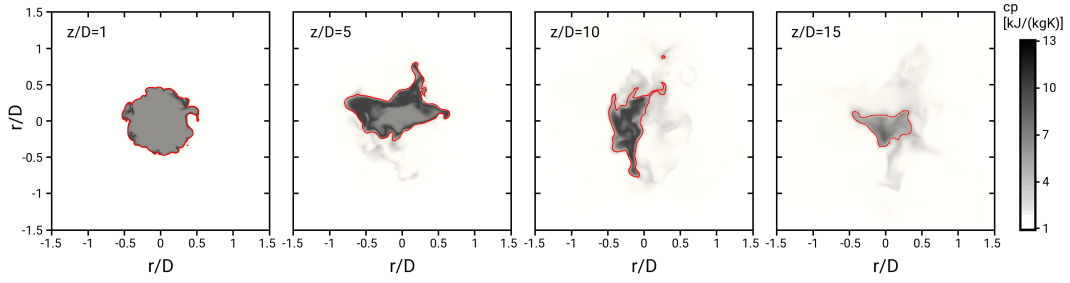


Figure 8: Isobaric heat capacity at four different cross sections,  $z/D = 1, 5, 10, 15$  for  $2.5t_c$  after the injection. Red isolines refer to the mean density between inlet and ambient nitrogen.

Close to the injection ( $z/D=1$ ), the jet is fairly circular with high heat capacities at the jet interface. Further downstream, the jet becomes stretched and the heat capacity tends to smear out. For ( $z/D \leq 10$ ), the heat capacity is approximately four times higher at the pseudo-boiling surface than that of the liquid-like jet. In this region, supplied thermal energy from the ambient nitrogen is primarily used to overcome intermolecular attraction, associated with a sharp change in the density. Thereby, a supercritical state transition takes place and the fluid absorbs heat without significantly raising the temperature. Further downstream ( $z/D > 10$ ), the pseudo-boiling surface is smeared out, and the temperature begins to increase.

#### 4.3. Mean flow properties

Figure 9 shows the variation of the averaged axial velocity along the centerline and against the radial distance, where  $r_{U,1/2}$  denotes the jet's half-width defined such that  $\tilde{U}(z/D, r_{U,1/2}) = 0.5 * \tilde{U}_c$ , where  $\tilde{U}_c$  is the local

value at the jet axis. For comparison, experimental data from an isothermal, subcritical round jet of Wyngnanski and Fiedler [47] are utilized.

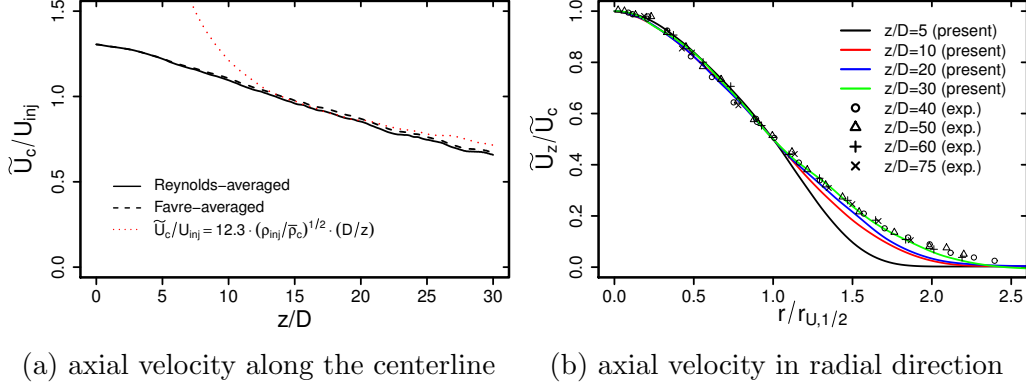


Figure 9: Variation of mean axial velocity along the centerline (a) and against radial distance (b). Comparison with measurements from a subcritical round jet of Wyngnanski and Fiedler [47].

With increasing axial distance, the axial velocity decays gradually and the jet spreads in radial direction. In the case of variable density jet flow, dimensional analysis and conservation of momentum imply that beyond the developing region  $\bar{U}_c/U_{inj} = B_U \cdot (\rho_{inj}/\bar{\rho}_c)^{1/2} \cdot D/z$ , where  $B_U$  is an empirical constant. In the present study,  $B_U = 12.3$ , which is approximately twice the velocity decay rate of subcritical jets. Regarding normalized mean axial velocity plotted against  $r/r_{U,1/2}$ , profiles collapse onto a single curve for  $z/D \geq 20$  and become self-similar. Thereby, the shape of the profiles are in excellent agreement with that of isothermal, subcritical round jets.

Regarding scalar quantities, figure 10 depicts the mean density along the centerline and radial profiles at different axial locations, where  $r_{\rho,1/2}$  is defined such that  $\bar{\rho}(z/D, r_{\rho,1/2}) = 0.5 \cdot (\bar{\rho}_c + \rho_\infty)$ .

Close to the injection, density remains approximately constant, decreases rapidly while the jet disintegrates ( $5 < z/D < 15$ ) and subsequently tends to the value of ambient density. In comparison to the measurements of Mayer et al. (2003) [1], the overall agreement is excellent, however, due to a lower Re-number in the present study, the jet breaks up slightly earlier. In accordance to the axial velocity, density profiles plotted against  $r/r_{\rho,1/2}$  collapse onto a single curve beyond  $z/D \approx 20$  and become self-similar as well. Thereby, shapes of the profiles are slightly steeper than the experimental ones.

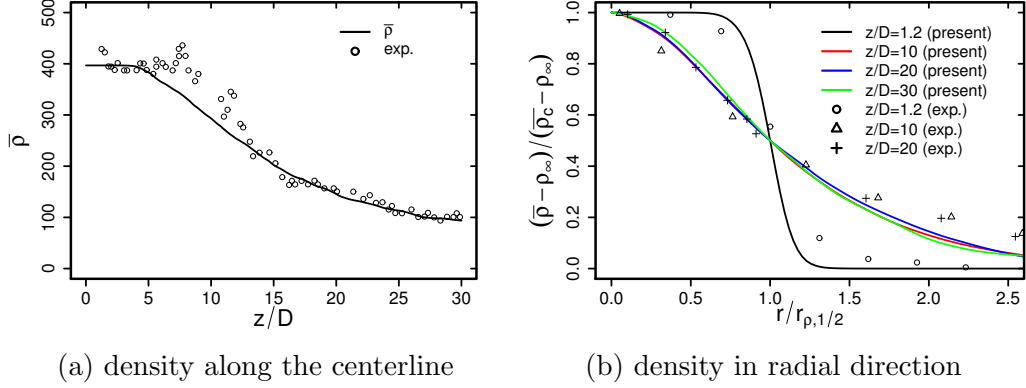


Figure 10: Predicted mean density along the centerline (a) and against radial distance (b). Comparison with measurements of a supercritical round jet of Mayer et al. (2003) [1].

Next, the spreading rate of the jet, quantified by the jet's half-widths of density, velocity and temperature as well as by the 50% location values of the density (full width half maximum, FWHM), are displayed in figure 10.

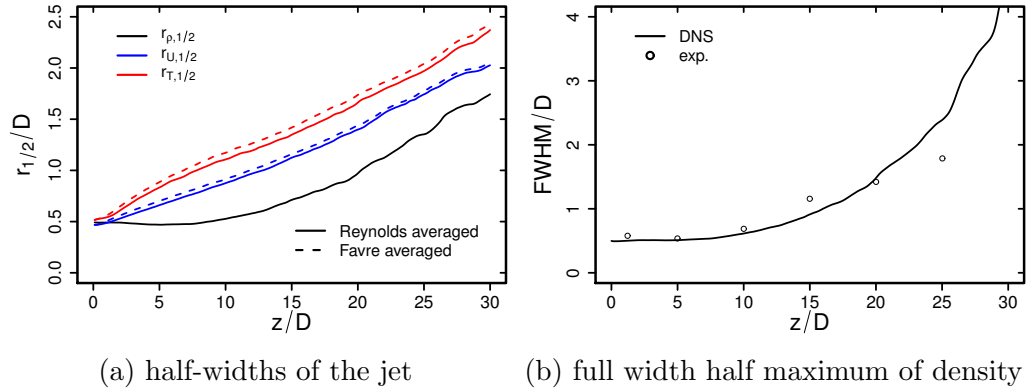


Figure 11: Spreading rate of the cryogenic jet; (a) jet's half-widths and (b) 50% location values of the density FWHM (full width half maximum) compared with measurements from a cryogenic round nitrogen jet of Mayer et al. (2003) [1].

As expected, the values of jet's half-widths are approximately  $0.5D$  close to the injection and increase with axial distance. Regarding the density,  $r_{\rho,1/2}$  remains constant up to  $z/D \approx 10$  followed by a linear increase. In contrast,  $r_{U,1/2}$  and  $r_{T,1/2}$  increase immediately after the injection. Highest half-widths occur in the case of temperature, implying that propagation of heat is more

dominant than momentum transport. In accordance with the measurements of Mayer et al. (2003) [1], the FWHM value remains constant at the injection region and increases for  $z/D > 10$ . The results of the numerical simulation are very close to the experimental data, even though the Reynolds number is significantly lower in the present study. Finally, based on the half-widths, the spreading rates of the jet  $S \equiv dr_{1/2}(z)/dz$  for  $z/D > 15$  are  $S_U = 0.063$  for the velocity,  $S_T = 0.067$  for the temperature and  $S_\rho = 0.074$  for the density. These values are significantly smaller than those of isothermal, subcritical jets ( $S_U \approx 0.096$ ).

#### 4.4. Turbulence dynamics

To gain further insight in the turbulence dynamics of disintegration processes at supercritical conditions, turbulence intensities, budget of turbulent kinetic energy, velocity spectra and turbulence scales are examined. As shown in the grid sensitivity study (see section 4.1), grid 3 also enables grid independent turbulence statistics. In the remaining part, it is therefore selected instead of grid 4 for sufficiently long-term statistics within a reasonable computational effort.

Starting with turbulence intensities, figure 12 displays profiles of the local root-mean-square of the turbulent velocity and density fluctuations along the jet axis and in radial direction.

In the case of rms velocity along the centerline,  $u_{rms}/\widetilde{U}_c$  remains approximately constant for  $z/D < 5$  and increases while the jet breaks up. In contrast to subcritical jets, in which rms velocity is about 25% of the mean after the developing region [48],  $u_{rms}/\widetilde{U}_c$  is clearly reduced and does not reach a constant value. Similarly, profiles of  $u_{rms}/\widetilde{U}_c$  plotted against  $r/r_{U,1/2}$  rise with increasing axial distance and do not collapse. Thus, in contrast to subcritical jets [52], the Reynolds stresses are not self-similar up to  $z/D = 30$ .

Regarding root-mean-square density along the centerline as shown in figure 12 (c), three stages associated with the jet disintegration process can be distinguished. In the first stage, close to the injection ( $z/D < 3$ ), the density fluctuations are zero and the liquid-like core is almost unaffected by the surrounding. In the second disintegration stage ( $3 < z/D < 12$ ), instabilities occur and dense pockets of liquid-like nitrogen are separated from the jet core, which leads to high density fluctuations. In the last stage ( $z/D > 18$ ), pockets break up and tend to smear out. Consequently, the density fluctuations decrease and tend asymptotically to zero. In terms of root-mean-square density plotted against  $r/r_{\rho,1/2}$ , peak values are shifted towards the jet's axis

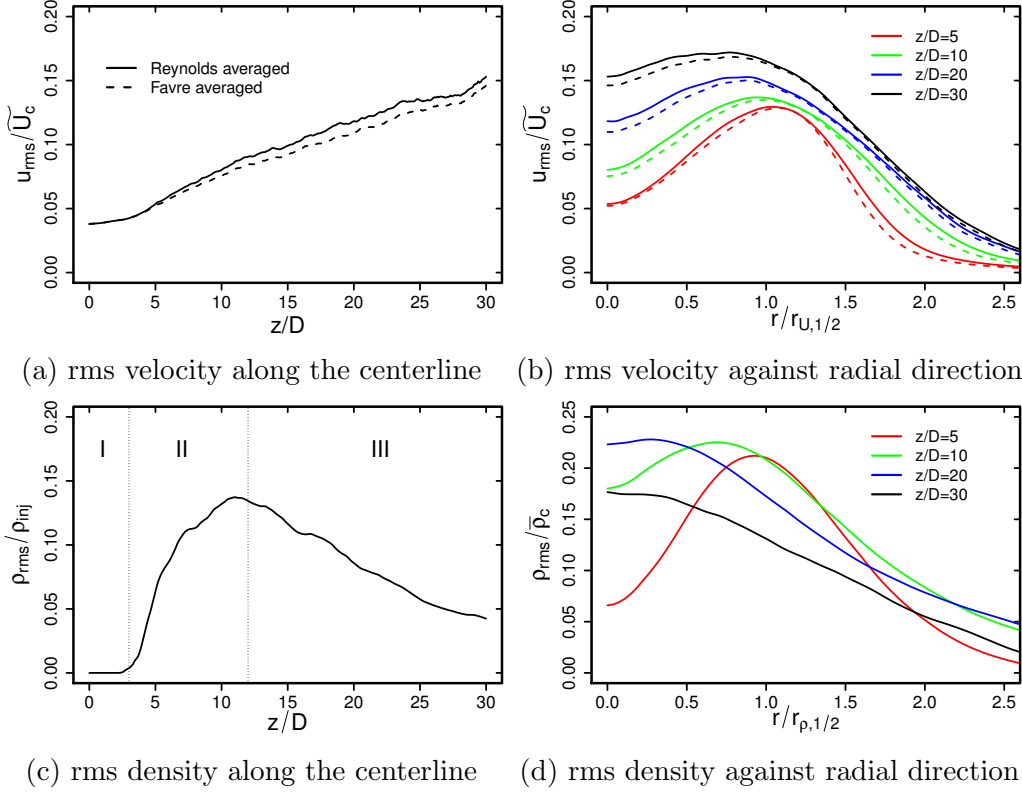


Figure 12: Variation of root-mean-square velocity and density fluctuations along the centerline (a),(c) and against radial distance (b),(d).

with increasing axial distance. Profiles do not collapse and no self-similarity behavior could be identified.

Next, the budget of turbulent kinetic energy (tke)  $\tilde{k} = \widetilde{u_i''u_i''}/2$  is investigated. Following the procedure of Huang et al. [59], the Favre-averaged turbulent kinetic energy equation can be written as:

$$\begin{aligned} \frac{D\tilde{\rho}\tilde{k}}{Dt} &= P + T_d + T_p + D + \epsilon + M + \Pi_d, \\ P &= -\tilde{\rho}\widetilde{u_i''u_j''}\frac{\partial\tilde{U}_i}{\partial x_j}, \quad T_d = -\frac{\partial}{\partial x_j}\left(\frac{1}{2}\tilde{\rho}\widetilde{u_i''u_i''u_j''}\right), \quad T_p = -\frac{\partial}{\partial x_j}(\overline{u_j'p'}), \\ D &= \frac{\partial}{\partial x_j}(\overline{u_i'\tau_{ij}'}), \quad \epsilon = -\overline{\tau_{ij}'\frac{\partial u_i'}{\partial x_j}}, \quad M = \overline{u_i''}\left(\frac{\partial\overline{\tau_{ij}}}{\partial x_j} - \frac{\partial\overline{p}}{\partial x_i}\right), \quad \Pi_d = \overline{p'\frac{\partial u_j'}{\partial x_j}}, \end{aligned} \quad (12)$$

where  $P$  denotes the production,  $T_d$  the turbulent diffusion due to third order moment,  $T_p$  the turbulent diffusion due to pressure transport,  $D$  the viscous diffusion,  $\epsilon$  the energy dissipation rate,  $M$  the mass flux contribution associated to density fluctuations and  $\Pi_d$  the pressure dilatation (pressure-shear correlation) term. Budget terms of the supercritical nitrogen jet along the centerline and against radial distance are shown in figure 13. The contribution terms along the centerline are normalized using  $U_{inj}$ ,  $\rho_{inj}$  and the pipe diameter, while radial profiles are normalized by  $U_c$ ,  $\rho_c$  and  $r_{U,1/2}$ .

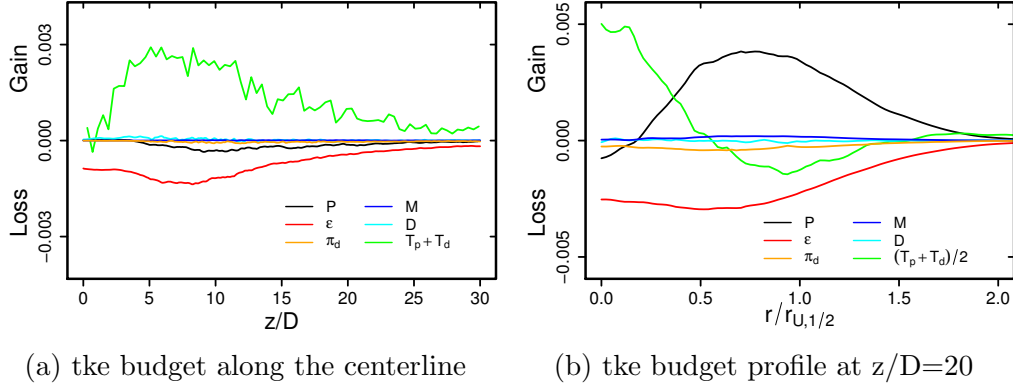


Figure 13: Turbulent kinetic energy budget along the centerline (a) and against radial direction (b). Quantities along the centerline are normalized by  $U_{inj}$ ,  $\rho_{inj}$  and the pipe diameter, while radial profiles are normalized by  $U_c$ ,  $\rho_c$  and  $r_{U,1/2}$ .

Throughout the jet's axis, turbulent diffusion is the dominant term, with dissipation being approximately half as large and with a relatively small amount of production. Other budget terms are negligible on the centerline. In the case of dissipation and production, both exhibit negative peak values at the jet breakup and increase further downstream. Regarding radial profiles, production increases in radial direction and peaks at  $r/r_{U,1/2} \approx 0.8$ , where  $P/\epsilon \sim 1.5$ , which is considerably higher than typical values of subcritical jets ( $P/\epsilon \sim 0.8$  [48]). Close to the jet's axis ( $r/r_{U,1/2} < 0.2$ ), production is negative, while turbulent diffusion dominates and transports energy toward the jet's axis. Dissipation remains constant below  $r/r_{U,1/2} < 0.8$  and subsequently tends to zero. The balance of turbulent kinetic energy observed is substantially different to those of subcritical, isothermal jets, especially in the case of production. Since shear stresses are zero at the jet's axis, production on the centerline is only due to the term  $-\bar{\rho} \left( \overline{u_z'' u_z''} \frac{\partial \bar{U}_z}{\partial z} + \overline{u_r'' u_r''} \frac{\partial \bar{U}_r}{\partial r} \right)$ ,

where  $\partial \widetilde{U}_z / \partial z < 0$  and  $\partial \widetilde{U}_r / \partial r > 0$ . While the jet disintegrates ( $z/D > 3$ ), the density decreases due to pseudo-boiling effects which leads to dilatation in radial and axial direction. At this stage,  $|\partial \widetilde{U}_z / \partial z| < |\partial \widetilde{U}_r / \partial r|$ , which causes a negative production term. Further downstream, this trend is slowly reversed until gas-like thermodynamic state is reached. Just as unusual is the dominance of turbulent diffusion around the jet's axis and the relatively small amount of dissipation.

Figure 14 shows the one-dimensional Eulerian frequency spectra of the axial and radial velocity component at the centerline. Fixed probes at  $z/D=5$  and 30 are selected, corresponding to the jet breakup and self-similarity region, respectively. Local values of jet half-width  $r_{U,1/2}$ , Reynolds stress  $\overline{u'_z u'_z}$  and centerline velocity  $\overline{U}_c$  are used to normalize the spectra, where  $f$  is the frequency. Dotted lines are the  $f^{-5/3}$  power curves, associated with the gradient of the inertial range.

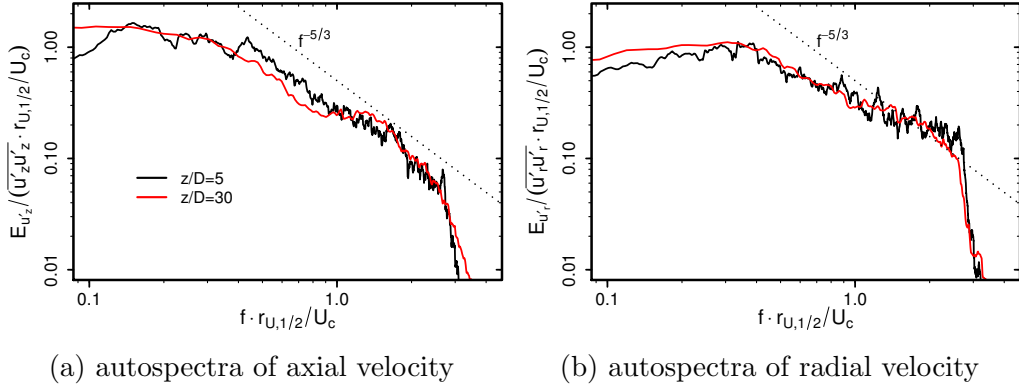


Figure 14: Normalized one-dimensional Eulerian autospectra of axial (a) and radial (b) velocity at the jet's centerline.

Similar to subcritical jets (see [52]), normalized energy curves of the axial velocity components exhibit a well developed inertial range and collapse onto a single curve at different axial locations. Minor deviations from ideal scaling of  $f^{-5/3}$  occur for higher frequencies. Like the axial velocity components, normalized autospectra of lateral velocity collapse onto a single curve and become self-similar. However, more of the turbulent kinetic energy is expressed in higher frequencies than in the subcritical case and the scaling differ from  $f^{-5/3}$ , which might be caused by anisotropic effects. Finally, integral length scales estimated by means of Taylor's hypothesis [60] are  $\sim 0.4 * r_{U,1/2}$  along

the centerline, which is in good agreement with those found in isothermal, subcritical round jets (see e.g. [47]).

#### 4.5. Heat transport

In this section, heat transport effects as they appear in supercritical injections are examined. First, normalized temperature  $\Theta = (T - T_\infty)/(\tilde{T}_c - T_\infty)$  and molecular Prandtl number ( $Pr = \mu c_p/\lambda$ ) profiles are provided in figure 15.

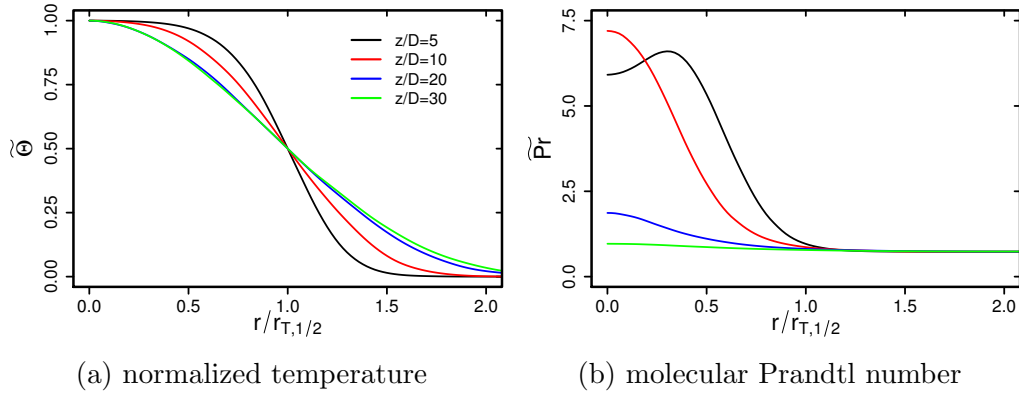


Figure 15: Normalized temperature (a) and molecular Prandtl number (b) plotted against radial distance at  $z/D=5, 10, 20$  and  $30$ .

As expected, normalized temperature equals one at the jet's axis and decreases in radial direction. With increasing axial distance, profiles smear out and enlarge in radial direction. Similar to the mean density (see figure 10b), normalized profiles collapse onto a single curve for  $z/D \geq 20$  and become self-similar. Regarding molecular Pr-number, radial profiles are high at jet's axis and decrease in radial direction. Highest Pr-numbers occur at the interface between cold liquid-like jet and warm gas-like ambient nitrogen, due to poor thermal diffusivity and high isobaric heat capacities at this region. Thereby, heat transport is inhibited and thermodynamic effects shield the cold jet from the ambient nitrogen, which impedes the disintegration process.

In figure 16, turbulent heat transport and its dependency on the mean temperature gradients is examined. Axial (a) and radial (b) dimensionless turbulent heat fluxes at  $z/D=5, 10, 20$  and  $30$  are presented.

Both, axial and radial heat fluxes increase in radial direction, reach their maximum at  $r/r_{T,1/2} \approx 0.9$  and afterwards tend to zero. With increasing



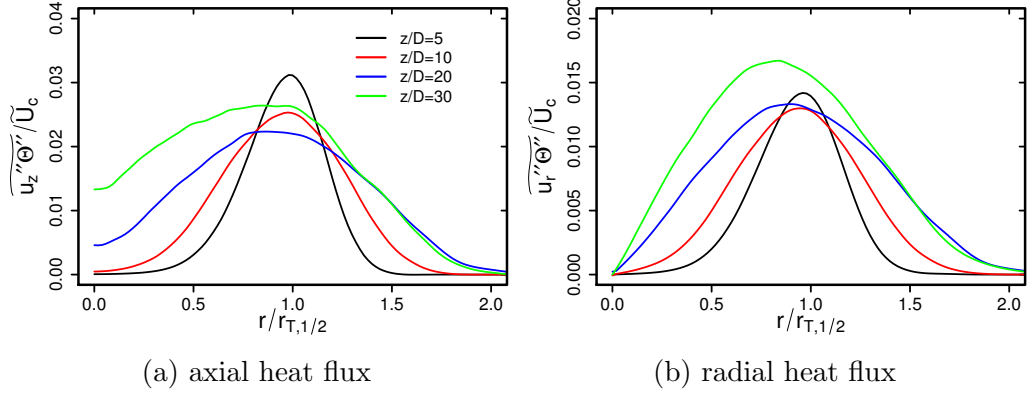


Figure 16: Axial and radial turbulent heat fluxes against radial direction at different axial positions:  $z/D=5, 10, 20$  and  $30$ .

axial distance, the profiles enlarge and peak values are shifted slightly towards the jet's axis. Higher values occur in the case of axial fluxes due to larger axial velocity fluctuations, whereby radial fluxes are approximately two times lower ( $\overline{u_z''\Theta''} \approx 2 * \overline{u_r''\Theta''}$ ). This finding is in line with results of experimental studies of subcritical jets [61, 62].

Regarding mean temperature gradients, absolute values of axial and radial profiles against radial distance are compared in figure 17 (a). Radial profiles at  $z/D=5$  are depicted. Corresponding peak values at different axial locations are shown in figure 17 (b).

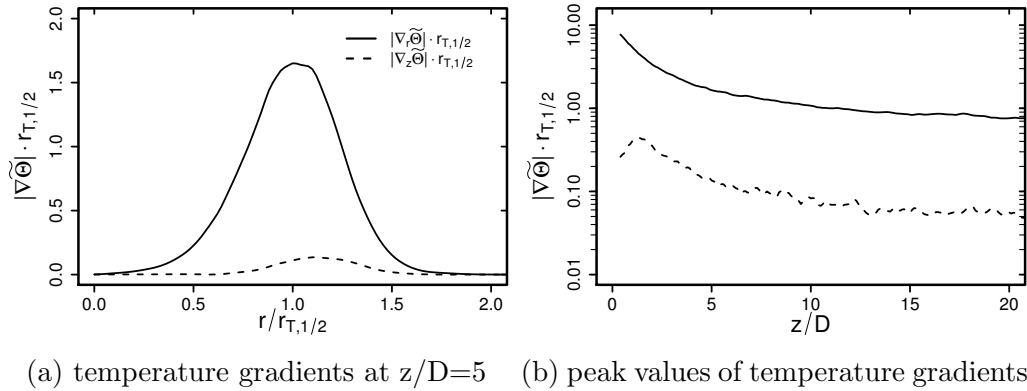


Figure 17: Normalized absolute temperature gradients at  $z/D=5$  (a) and their peak values (b) at different axial locations.

Just as with the turbulent heat fluxes, mean temperature gradients increase in radial direction, exhibit a peak value at  $r/r_{T,1/2} \approx 1$  and decrease subsequently. Thereby, normalized peak values decrease downstream and tend asymptotically to a constant value. However, it appears that radial mean temperature gradients are considerable steeper than axial ones ( $|\nabla_r \Theta| \approx 10 * |\nabla_z \Theta|$ ). This is in contradiction with the linear isotropic eddy diffusivity hypothesis

$$\widetilde{u''_i \Theta''} = -\alpha_t \frac{\partial \widetilde{\Theta}}{\partial x_i}, \quad (13)$$

which states that turbulent heat transport is proportional to the corresponding mean temperature gradient, with turbulent heat diffusivity  $\alpha_t$  as a proportional factor. The opposite is true in the present case. In fact, equation 13 implies that  $\widetilde{u''_z \Theta''} * \partial \widetilde{\Theta} / \partial r = \widetilde{u''_r \Theta''} * \partial \widetilde{\Theta} / \partial z$ . However, it is found that  $\widetilde{u''_z \Theta''} * \partial \widetilde{\Theta} / \partial r$  is approximately 20 times larger than  $\widetilde{u''_r \Theta''} * \partial \widetilde{\Theta} / \partial z$ . This suggests, that tensorial heat diffusivity models might be appropriate for such supercritical flows as proposed in [63, 64, 65, 66, 67] and others from investigations in subcritical applications.

## 5. Conclusion

Direct numerical simulation of a round jet of cryogenic nitrogen, which mimics the experiment by Mayer et al. (2003) [1] in terms of geometry, thermodynamics, and hydrodynamics, but at reduced Reynolds number ( $Re=5300$  based on the injection diameter), has been conducted. Real fluid equation of state, realistic inflow turbulence and generalized transport property models were included and evaluated. Thereby, turbulence statistics, physical mechanisms that dominate the flow dynamics and heat transport phenomena have been investigated in terms of energy spectra, first and second statistical moments for the flow field, turbulent kinetic energy budget, jet spreading rate, Pr-number and temperature distribution along with turbulent heat flux. Finally, a link to modeling of the heat flux vector has been established, and the suitability of some existing heat flux models as employed in such supercritical fluid flows has been examined.

Within this study, specific aspects characterizing the disintegration process of turbulent jets at supercritical conditions have been pointed out. Especially the pseudo-boiling effects have been clearly established. Considering the density fluctuation evolution along the centerline, three main stages of

jet disintegration could be recognized and associated with the mixing process. The parameter regimes advantageous to mixing have been determined as those lying between  $12 < z/D < 25$ , where the density fluctuations tend asymptotically to zero, the Pr-number strongly decreases while the temperature increases rapidly.

Regarding turbulence dynamics, Reynolds stresses along with the balance of turbulent kinetic energy are substantially different compared to subcritical, isothermal jets. Normalized Reynolds stresses are clearly reduced and do not collapse on a single curve, while mean statistics are self-similar beyond  $z/D = 20$ . Throughout the jet's axis, turbulent diffusion is the dominant term in the turbulent kinetic energy budget, with dissipation being approximately half as large and with a relatively small amount of production. While the jet disintegrates, density decreases rapidly, which leads to a dilatation in radial and axial direction. Thereby negative production occurs around the jet's axis. Moreover, peak values of  $P/\epsilon \sim 1.5$  arise, which are considerably higher than typical values of subcritical jets ( $P/\epsilon \sim 0.8$  [48]).

Examining the heat transport and its dependency on the mean temperature gradients, it appears that radial mean temperature gradients are considerably steeper than axial ones, even though axial turbulent heat fluxes are significantly higher. This is in contradiction with the linear isotropic eddy diffusivity hypothesis, which states that turbulent heat transport is proportional to the corresponding mean temperature gradient. This suggests, that tensorial heat diffusivity models might be appropriate for such supercritical flows as proposed in [63, 64, 65, 66, 67] and others for subcritical flow cases.

Finally, the present work provides a comprehensive database that is difficult to obtain experimentally at such extreme thermodynamic conditions. This data may support the development and validation of models either in RANS or in LES context.

## 6. Acknowledgement

The authors gratefully acknowledge the financial support by the DFG (German Research Council) SFB-TRR 75 and the support of the numerical simulations on the Lichtenberg High Performance Computer (HHLR) at the University of Darmstadt. We also gratefully acknowledge the cooperation with Prof. Dr. rer. nat. Michael Pfitzner, especially with Dr.-Ing. Hagen Müller, from the department of thermodynamics at the Universität der Bundeswehr München.

- [1] W. Mayer, J. Telaar, R. Branam, G. Schneider, J. Hussong, Raman measurements of cryogenic injection at supercritical pressure, *Heat and Mass Transfer* 39 (2003) 709–719. doi:10.1007/s00231-002-0315-x.
- [2] E. Messerschmid, S. Fasoulas, *Raumfahrtsysteme*, 4th Edition, Springer-Verlag Berlin Heidelberg, 2011. doi:10.1007/978-3-642-12817-2\_1.
- [3] Ž. Knez, E. Markočič, M. Leitgelb, M. Primožič, M. Knez Hrnčič, M. Škerget, Industrial applications of supercritical fluids: a review, *Energy* 77 (2014) 235–243. doi:10.1016/j.energy.2014.07.044.
- [4] Y. Ahn, S. J. Bae, M. Kim, S. K. Cho, S. Baik, J. I. Lee, J. E. Cha, Review of supercritical  $CO_2$  power cycle technology and current status of research and development, *Nucl. Eng. Technol.* 47 (2015) 647–661. doi:10.1016/j.net.2015.06.009.
- [5] D. T. Banuti, M. Raju, P. C. Ma, M. Ihme, J. P. Hickey, Seven questions about supercritical fluids - towards new fluid state diagram, *AIAA SciTech Forum*.doi:10.2514/6.2017-1106.
- [6] D. T. Banuti, Crossing the Widom-line - Supercritical pseudo-boiling, *J. of Supercritical Fluids* 98 (2015) 12–16. doi:10.1016/j.supflu.2014.12.019.
- [7] M. Oswald, A. Schik, Supercritical nitrogen free jet investigated by spontaneous Raman scattering, *Experiments in Fluids* 27 (1999) 497–506. doi:10.1007/s003480050374.
- [8] W. Mayer, H. Tamura, Propellant injection in a liquid oxygen/gaseous hydrogen rocket engine, *Journal of Propulsion and Power* 12 (6) (1996) 1137–1147. doi:10.2514/3.24154.
- [9] M. Oswald, J. J. Smith, R. Branam, J. Hussong, A. Schik, B. Chehroudi, D. Talley, Injection of fluids into supercritical environment, *Combust. Sci. and Tech.* 178 (2006) 49–100. doi:10.1080/00102200500292464.
- [10] S. Candel, M. Juniper, G. Singla, P. Scoufflaire, C. Rolon, Structure and dynamics of cryogenic flames at supercritical pressure, *Combust. Sci. and Tech.* 178 (2006) 161–192. doi:10.1080/00102200500292530.

- [11] M. Habiballah, M. Orain, F. Grisch, L. Vingert, P. Gicquel, Experimental studies of high-pressure cryogenic flames on the mascotte facility, *Combust. Sci. and Tech.* 178 (2007) 101–128. doi:10.1080/00102200500294486.
- [12] J. Oefelein, V. Yang, Modeling high-pressure mixing and combustion processes in liquid rocket engines, *Journal of Propulsion and Power* 14 (5) (1998) 843–857. doi:10.2514/2.5349.
- [13] J. Oefelein, Mixing and combustion of cryogenic oxygen-hydrogen shear-coaxial jet flames at supercritical pressure, *Combust. Sci. and Tech.* 178 (2006) 229–252. doi:10.1080/00102200500325322.
- [14] J. Bellan, Theory, modeling and analysis of turbulent supercritical mixing, *Combust. Sci. and Tech.* 178 (2006) 253–281. doi:10.1080/00102200500292241.
- [15] N. Zong, V. Yang, Cryogenic fluid jets and mixing layers in transcritical and supercritical environments, *Combust. Sci. and Tech.* 178 (2006) 193–227. doi:10.1080/00102200500287613.
- [16] J. Sierra-Pallares, J. García del Valle, P. García-Carrascal, F. Castro Ruiz, Numerical study of supercritical and transcritical injection using different Prandtl numbers: a second law analysis, *J. of Supercritical Fluids* 115 (2016) 86–98. doi:10.1016/j.supflu.2016.05.001.
- [17] T. Kim, Y. Kim, S. K. Kim, Numerical study of cryogenic liquid nitrogen jets at supercritical pressures, *J. of Supercritical Fluids* 56 (2) (2011) 152–163. doi:10.1016/j.supflu.2010.12.008.
- [18] X. Petit, G. Ribert, G. Lartigue, P. Domingo, Large-eddy simulation of supercritical fluid injection, *J. of Supercritical Fluids* 84 (2013) 61–73. doi:10.1016/j.supflu.2013.09.011.
- [19] T. Schmitt, L. Selle, A. Ruiz, B. Cuenot, Large-eddy simulation of supercritical pressure round jets, *AIAA Journal* 48 (9) (2010) 2133–2144. doi:10.2514/1.J050288.
- [20] H. Müller, C. A. Niedermeier, J. Matheis, M. Pfitzner, S. Hickel, Large-eddy simulation of nitrogen injection at trans- and supercritical conditions, *Physics of Fluids* 28 (2016) 015102. doi:10.1063/1.4937948.

- [21] R. Mari, B. Cuenot, F. Duchaine, L. Selle, Stabilization mechanisms of a supercritical hydrogen/oxygen flame, Center for Turbulence Research, Proceedings of the Summer Program (2012) 439–449.
- [22] H. Huo, V. Yang, Large-eddy simulation of supercritical combustion: model validation against gaseous H<sub>2</sub>-O<sub>2</sub> Injector, Journal of Propulsion and Power (2017) 1–13.doi:10.2514/1.B36368.
- [23] N. Tramecourt, S. Menon, J. Amaya, LES of supercritical combustion in a gas turbine engine, 40th AIAA/ASME/SAE/ASEE Joint Propulsion Conference and Exhibit, Joint Propulsion Conferences (2004) 1–11.doi:10.2514/6.2004-3381.
- [24] L. Selle, G. Ribert, Modeling requirements for large-eddy simulation of turbulent flows under supercritical thermodynamic conditions, Center for Turbulence Research, Proceedings of the Summer Program 2008 (2008) 195–207.doi:10.1.1.169.9029.
- [25] L. Selle, S. T., Large-eddy simulation of single-species flows under supercritical thermodynamic conditions, Combust. Sci. and Tech. 182 (2010) 392–404. doi:10.1080/00102200903462664.
- [26] N. A. Okong’o, J. Bellan, Entropy production of emerging turbulent scales in a temporal supercritical n-heptane/nitrogen three-dimensional mixing layer, Proceedings of the Combustion Institute 28 (1) (2000) 497–504. doi:10.1016/S0082-0784(00)80248-9.
- [27] R. S. Miller, K. G. Harstad, J. Bellan, Direct numerical simulations of supercritical fluid mixing layers applied to heptane-nitrogen, J. Fluid Mech. 436 (2001) 1–39. doi:10.1.1.470.3819.
- [28] N. A. Okong’o, J. Bellan, Direct numerical simulations of transitional supercritical binary mixing layers: heptane and nitrogen, J. Fluid Mech. 464 (2002) 1–34. doi:10.1017/S0022112002008480.
- [29] L. Selle, N. Okong’o, J. Bellan, H. K., Modelling of subgrid-scale phenomena in supercritical transitional mixing layers: an a priori study, J. Fluid Mech. 593 (2007) 57–91. doi:10.1017/S0022112007008075.

- [30] J. Foster, R. Miller, A priori analysis of subgrid mass diffusion vectors in high pressure turbulent hydrogen/oxygen reacting shear layer flames, *Physics of Fluids* 24 (2012) 075114. doi:10.1063/1.4739065.
- [31] E. Taskinoglu, J. Bellan, A posteriori study using a DNS database describing fluid disintegration and binary-species mixing under supercritical pressure: heptane and nitrogen, *J. Fluid Mech.* 645 (2010) 211–254. doi:10.1017/S0022112009992606.
- [32] A. Ruiz, G. Lacaze, J. Oefelein, R. Mari, B. Cuenot, L. Selle, T. Poinso, Numerical benchmark for high-Reynolds-number supercritical flows with large density gradients, *AIAA Journal* 54 (5) (2016) 1445–1460. doi:10.2514/1.J053931.
- [33] B. Chehroudi, D. Talley, A. Coy, Visual characteristics and initial growth rates of round cryogenic jets at subcritical and supercritical pressures, *Physics of Fluids* 14 (2) (2002) 850. doi:10.1063/1.1430735.
- [34] S. Candel, G. Herding, R. Snyder, P. Scouffaire, C. Rolon, L. Vingert, M. Habiballah, F. Grisch, M. Péalat, P. Bouchardy, D. Stepowski, A. Cessou, P. Colin, Experimental investigation of shear coaxial cryogenic jet-flame, *Journal of Propulsion and Power* 14 (5) (1998) 826–834. doi:10.2514/2.5346.
- [35] O. J. Haidn, M. Habiballah, Research on High Pressure Cryogenic Combustion, *Aerospace Science and Technology* 7 (6) (2003) 473–791. doi:10.1016/S1270-9638(03)00052-X.
- [36] N. Guezennec, M. Masquelet, S. Menon, Large eddy simulation of flame-turbulence interactions in a LOX-CH<sub>4</sub> shear coaxial injector, 50th AIAA Aerospace Sciences Meeting including the New Horizons Forum and Aerospace Exposition, *Aerospace Sciences Meetings* 2012–1267. doi:10.2514/6.2012-1267.
- [37] J. H. Bae, J. Y. Yoo, Direct numerical simulation of turbulent supercritical flows with heat transfer, *Physics of Fluids* 17 (10) (2005) 105104. doi:10.1063/1.2047588.
- [38] D. Y. Peng, D. P. Robinson, A new two-constant equation of state, *Ind. Eng. Chem. Fundam.* 15 (1) (1976) 59–64. doi:10.1026/l160057a011.

- [39] P. M. Mathias, T. Naheiri, E. M. Oh, A density correction for the Peng-Robinson equation of state, *Fluid Phase Equilibria* 47 (1) (1989) 77–87. doi:10.1016/0378-3812(89)80051-2.
- [40] A. M. Abudour, S. A. Mohammad, R. L. Robinson Jr., K. A. M. Gasem, Volume-translated Peng-Robinson equation of state for saturated and single-phase liquid densities, *Fluid Phase Equilibria* 335 (2012) 74–87. doi:10.1016/j.fluid.2012.08.013.
- [41] T. H. Chung, M. Ajlan, L. L. Lee, K. E. Starling, Generalized multi-parameter correlation for nonpolar and polar fluid transport properties, *Ind. Eng. Chem. Res.*, 27 (4) (1988) 671–679. doi:10.1021/ie00076a024.
- [42] R. I. Issa, Solution of the implicitly discretised fluid flow equations by operator-splitting, *J. of Computational Physics* 62 (1) (1985) 40–65. doi:doi.org/10.1016/0021-9991(86)90099-9.
- [43] S. Patankar, D. Spalding, A calculation procedure for heat, mass and momentum transfer in three-dimensional parabolic flows, *Int. J. of Heat and Mass Transfer* 15 (10) (1972) 1787–1806. doi:10.1016/0017-9310(72)90054-3.
- [44] H. Jasak, Error Analysis and Estimation for Finite Volume Method with Applications to Fluid Flows, Ph.D. thesis, Imperial College of Science, Technology and Medicine (1996).
- [45] P. L. Roe, Characteristic-based schemes for the euler equations, *Ann. Rev. Fluid Mech.* 18 (1986) 337–365. doi:10.1146/annurev.fl.18.010186.002005.
- [46] OpenFOAM Programmer’s Guide, 2nd Edition (2015).
- [47] I. Wagnanski, H. Fiedler, Some measurements in the self-preserving jet, *J. Fluid Mech.* 38 (3) (1969) 577–612. doi:10.1017/S0022112069000358.
- [48] N. R. Panchapakesan, J. L. Lumley, Turbulence measurements in axisymmetric jets of air and helium. Part 1. air jet, *J. Fluid Mech.* 246 (1993) 197–223. doi:10.1017/S0022112093000096.



- [49] H. J. Hussein, S. P. Capp, W. K. Georg, Velocity measurements in a high-Reynolds-number, momentum-conserving, axisymmetric, turbulent jet, *J. Fluid Mech.* 258 (1994) 31–75. doi:10.1017/S002211209400323X.
- [50] B. J. Boersma, G. Brethouwer, F. T. M. Nieuwstadt, A numerical investigation on the effect of the inflow conditions on the self-similar region of a round jet, *Physics of Fluids* 10 (4) (1998) 899. doi:10.1063/1.869626.
- [51] B. J. Boersma, Numerical simulation of the noise generated by a low Mach number, low Reynolds number jet, *Fluid Dyn. Res.* 35 (6) (2004) 425–447. doi:10.1016/j.fluiddyn.2004.10.003.
- [52] Z. Wang, P. He, Y. Lv, J. Zhou, J. Fan, K. Cen, Direct numerical simulation of subsonic round turbulent jet, *Flow, Turbulence Combust* 84 (4) (2010) 669–686. doi:10.1007/s10494-010-9248-5.
- [53] C. Chin, A. S. H. Ooi, I. Marusic, H. M. Blackburn, The Influence of pipe length on turbulence statistics computed from direct numerical simulation data, *Physics of Fluids* 22 (11) (2010) 115107. doi:10.1063/1.3489528.
- [54] J. Ahn, J. L. Lee, H. J. Sung, Direct numerical simulations of fully developed turbulent pipe flows for  $Re_\tau=180$ , 544 and 934, *Int. J. Heat and Fluid Flow* 44 (2013) 222–228. doi:10.1016/j.ijheatfluidflow.2013.05.022.
- [55] P. J. Linstrom, W. G. Mallard, no. 69, 2016. [link].  
URL <http://webbook.nist.gov/chemistry/fluid>
- [56] R. Span, E. W. Lemmon, R. T. Jacobsen, W. Wagner, A. Yokozeki, A reference equation of state for the thermodynamic properties of nitrogen for temperatures from 63.151 to 1000 K and pressures to 2200 MPa, *J. Phys. Chem. Ref. Data* 29 (6) (2000) 1361–1433. doi:10.1063/1.1349047.
- [57] G. Grötzbach, Spatial resolution requirements for direct numerical simulation of the Rayleigh-Bérnard convection, *J. of Comp. Physics* 49 (2) (1983) 241–264. doi:10.1016/0021-9991(83)90125-0.
- [58] F. Battista, F. Picano, C. M. Casciola, Turbulent mixing of a slightly supercritical Van der Waals fluid at low-Mach number, *Physics of Fluids* 26 (2014) 055101. doi:10.1063/1.4873200.

- [59] P. Huang, G. Coleman, P. Bradshaw, Compressible turbulent channel flows: DNS results and modelling, *J. Fluid Mech.* 305 (1995) 185–218. doi:10.1017/S0022112095004599.
- [60] G. I. Taylor, The spectrum of turbulence, *Proc. R. Soc. London Ser. A* 164 (919) (1938) 476–490. doi:10.1098/rspa.1938.0032.
- [61] F. Lemoine, Y. Antoine, M. Wolff, M. Lebouche, Simultaneous temperature and 2D velocity measurements in a turbulent heated jet using combined laser-induced fluorescence and LDA, *Experiments in Fluids* 26 (4) (1999) 315–323. doi:10.1007/s003480050294.
- [62] H. Lee, B. Böhm, A. Sadiki, A. Dreizler, Turbulent heat flux measurement in non-reacting round jet, using BAM: $Eu^{2+}$  phosphor thermography and particle image velocimetry, *Appl. Phys. B* (2016) 122–209doi:10.1007/s00340-016-6484-y.
- [63] G. K. Batchelor, Diffusion in a field of homogeneous turbulence, *Aust. J. Sci. Res.* 2 (1949) 437–450.
- [64] B. J. Daly, F. H. Harlow, Transport equations in turbulence, *Phys. of Fluids* 13 (11) (1970) 2637–2649. doi:10.1063/1.1692845.
- [65] S. H. Peng, L. Davidson, On a subgrid-scale heat flux model for large eddy simulation of turbulent thermal flow, *Int. J. of Heat and Mass Transfer* 45 (7) (2002) 1393–1405. doi:10.1016/S0017-9310(01)00254-X.
- [66] B. A. Younis, C. G. Speziale, T. T. Clark, A rational model for the turbulent scalar fluxes, *Proc. R. Soc. A* 461 (2004) 575–594. doi:10.1098/rspa.2004.1380.
- [67] P. Pantangi, Y. Huai, A. Sadiki, Mixing analysis and optimization in jet mixer systems by means of large eddy simulation, *Micro and Macro Mixing: Analysis, Simulation and Numerical Calculation* (2010) 205–226doi:10.1007/978-3-642-04549-3.